

# Strain effects on topological and valley properties of Janus monolayer VSiGeN<sub>4</sub>

San-Dong Guo<sup>1</sup>, Wen-Qi Mu<sup>1</sup>, Jia-Hao Wang<sup>1</sup>, Yu-Xuan Yang<sup>1</sup>, Bing Wang<sup>2</sup> and Yee-Sin Ang<sup>3</sup>

<sup>1</sup>*School of Electronic Engineering, Xi'an University of Posts and Telecommunications, Xi'an 710121, China*

<sup>2</sup>*Institute for Computational Materials Science, School of Physics and Electronics, Henan University, 475004, Kaifeng, China and*

<sup>3</sup>*Science, Mathematics and Technology (SMT), Singapore University of Technology and Design (SUTD), 8 Somapah Road, Singapore 487372, Singapore*

Strain is an effective method to tune the electronic properties of two-dimension (2D) materials, and can induce novel phase transition. Recently, 2D MA<sub>2</sub>Z<sub>4</sub> family materials are of interest because of their emerging topological, magnetic and superconducting properties. Here, we investigate the impact of strain effects ( $a/a_0:0.96\sim 1.04$ ) on the physical properties of Janus monolayer VSiGeN<sub>4</sub> as a derivative of VSi<sub>2</sub>N<sub>4</sub> or VGe<sub>2</sub>N<sub>4</sub>, which possesses dynamical, mechanical and thermal stabilities. For out-of-plane magnetic anisotropy, with increasing strain, VSiGeN<sub>4</sub> undergoes transition between ferrovalley semiconductor (FVS), half-valley-metal (HVM), valley-polarized quantum anomalous Hall insulator (VQAH), HVM and FVS. These imply twice topological phase transitions, which are related with sign-reversible Berry curvature and band inversion between  $d_{xy}+d_{x^2-y^2}$  and  $d_{z^2}$  orbitals for K or -K valley. The band inversion also leads to transformation of valley splitting strength between valence and conduction bands. However, for in-plane magnetic anisotropy, no special quantum anomalous Hall (QAH) states and valley polarization exist within the considered strain range. The actual magnetic anisotropy energy (MAE) shows no special QAH and HVM states in monolayer VSiGeN<sub>4</sub>. Fortunately, these can be easily achieved by external magnetic field, which adjusts the easy magnetization axis of VSiGeN<sub>4</sub> from in-plane one to out-of-plane one. Our findings shed light on how strain can be employed to engineer the electronic states of VSiGeN<sub>4</sub>, which may open new perspectives for multifunctional quantum devices in valleytronics and spintronics.

Keywords: Strain, Magnetic anisotropy energy, Phase transition

Email:sandongyuwang@163.com

## I. INTRODUCTION

Magnetism of 2D systems is one of the most fascinating properties of material due to its interplay with the other important properties of materials such as superconductivity, ferrovalley (FV), ferroelectricity, piezoelectricity and QAH effects. However, based on Mermin-Wagner theorem, long-range magnetic order is prohibited in a 2D system<sup>1</sup>. Fortunately, 2D intrinsic long-range ferromagnetic (FM) order semiconductors, Cr<sub>2</sub>Ge<sub>2</sub>Te<sub>6</sub> and CrI<sub>3</sub>, have been achieved experimentally, obtained from their van der Waals (vdW) layered bulk materials<sup>2,3</sup>, due to the stabilization of FM order by magnetic anisotropy. In addition to this, the direction of magnetic anisotropy has important influence on the topological and valley properties of some 2D materials, because it can affect the symmetry of such 2D systems<sup>4-7</sup>. For example in monolayer RuBr<sub>2</sub>, FV to HVM to QAH to HVM to FV transitions can be induced by increasing the electron correlation  $U$  with a fixed out-of-plane magnetic anisotropy, but no special QAH states and valley polarization can be observed for the in-plane case<sup>7</sup>. Thus, it may be a very interesting to tune the magnetic anisotropy of 2D systems by external field, such as biaxial strain, electric field, and correlation effects.

Strain engineering is an important strategy for tuning the electronic, topological, thermoelectric, piezoelectric and magnetic properties of 2D materials, which has been widely used in the modulation of physical and chemical properties<sup>8</sup>. The QAH state in the VN<sub>2</sub>X<sub>2</sub>Y<sub>2</sub> nanosheets (X=B-Ga, Y=O-Te) can be induced by strain, and the

valley polarization can also be switched from the bottom conduction band to the top valence band<sup>9</sup>. For monolayer MBr<sub>2</sub> (M=Ru and Os), compressive strain can induce phase transitions in the materials from FVS to HVM to VQAH to HVM to FVS<sup>10</sup>. However, in these works, the intrinsic MAE as a function of strain has not been considered, and out-of-plane magnetic anisotropy is assumed to be fixed within the considered strain range. Our recent works show that an increasing strain can induce switching of the magnetic anisotropy from out-of-plane one to in-plane one<sup>7</sup>, thus producing manifold electronic states. Thus, strain engineering may produce complex phase transition of electronic states by tuning the magnetic anisotropy.

In 2020, the septuple-atomic-layer 2D MoSi<sub>2</sub>N<sub>4</sub> and WSi<sub>2</sub>N<sub>4</sub> have been successfully synthesized by the chemical vapor deposition method<sup>11</sup>. Subsequently, 2D MA<sub>2</sub>Z<sub>4</sub> family with a septuple-atomic-layer structure has been constructed by intercalating a MoS<sub>2</sub>-type monolayer MZ<sub>2</sub> into an InSe-type monolayer A<sub>2</sub>Z<sub>2</sub>, and the family possesses emerging topological, magnetic, valley, superconducting and electrical contact properties<sup>12-14</sup>. Then, Janus 2D materials in the new 2D MA<sub>2</sub>Z<sub>4</sub> family are proposed, such as MSiGeN<sub>4</sub> (M=Mo and W) and SrAlGaSe<sub>4</sub>, and some novel properties can be achieved in these Janus materials, such as Rashba spin splitting and out-of-plane piezoelectric polarizations<sup>15,16</sup>. Recently, Janus VSiGeN<sub>4</sub> monolayer is predicted to be a thermodynamically stable intrinsic 2D ferromagnet<sup>17</sup>.

In this work, we investigate strain effects on topological and valley properties of Janus VSiGeN<sub>4</sub> monolayer,

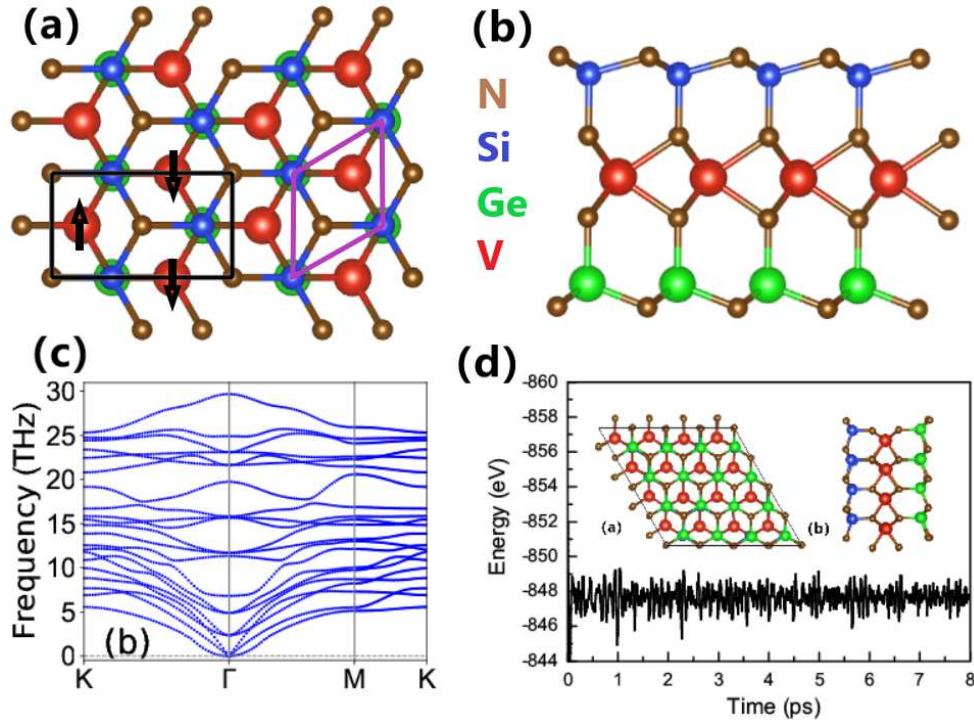


FIG. 1. (Color online) For VSiGeN<sub>4</sub> monolayer, (a): top view and (b): side view of crystal structure. The primitive (rectangle supercell) cell is shown by purple (black) lines, and the AFM configuration is marked with black arrows in (a). (c): the phonon dispersion curves. (d): the total energy fluctuations as a function of simulation time at 300 K, and insets show the final structures (top view (a) and side view (b)) of VSiGeN<sub>4</sub> after 8 ps at 300 K.

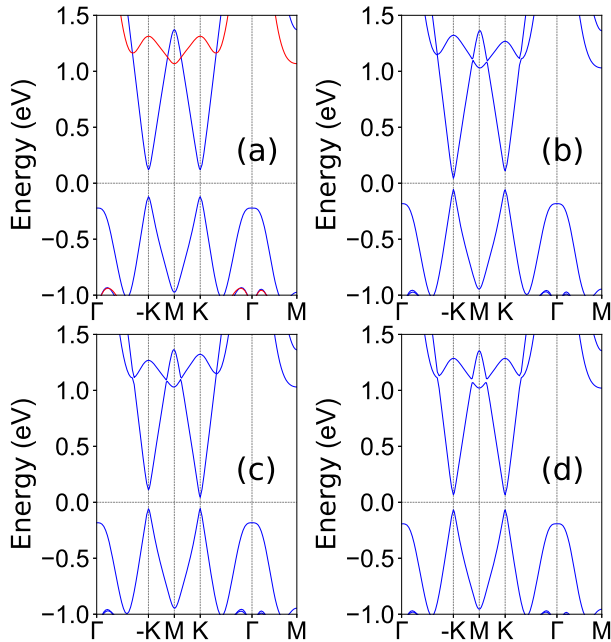


FIG. 2. (Color online) Energy band structures of VSiGeN<sub>4</sub> (a) without SOC; (b), (c) and (d) with SOC for magnetic moment of V along the positive  $z$ , negative  $z$ , and positive  $x$  direction, respectively. In (a), the blue (red) lines represent the band structure in the spin-up (spin-down) direction.

and reveal the importance of magnetic anisotropy in determining its magnetic, topological and valley properties. It is found that different strain strengths can drive the system into different novel electronic states (FVS, HVM and VQAHI) with fixed out-of-plane case, enabling a rich phase diagram. However, for in-plane case, only common magnetic states appear. Due to weak spin-orbit coupling (SOC) in VSiGeN<sub>4</sub>, the magnetic shape anisotropy (MSA) induced by the magnetic dipolar interaction can overcome the magnetocrystalline anisotropy (MCA) to evince an easy-plane in considered strain range. So, strained VSiGeN<sub>4</sub> is intrinsically a common magnetic semiconductor. However, these topological and valley states can be achieved by small external magnetic field. With increasing  $a/a_0$ , the MCA energy firstly switches from in-plane to out-of-plane. Further increasing  $a/a_0$  will drive two additional transitions in the MCA from out-of-plane to in-plane to out-of-plane. Several transitions in the MCA are further identified by calculating MCA versus  $U$ . Our works highlight the role of magnetic anisotropy for VSiGeN<sub>4</sub>, and deepen our understanding of strain along with magnetic anisotropy induced topological and valley states.

The rest of the paper is organized as follows. In the next section, we shall give our computational details and methods. In the next few sections, we shall present structure and stabilities, electronic states and strain effects on physical properties of VSiGeN<sub>4</sub> monolayer. Finally, we

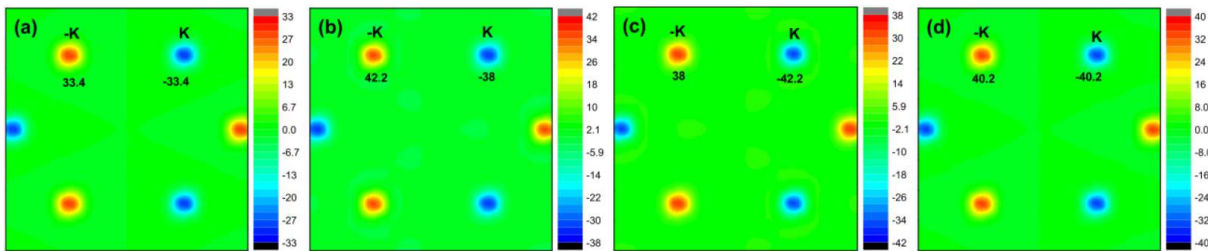


FIG. 3. (Color online) For VSiGeN<sub>4</sub> monolayer, the corresponding Berry curvature distribution in 2D BZ (a) without SOC; (b), (c) and (d) with SOC for magnetic moment of V along the positive  $z$ , negative  $z$ , and positive  $x$  direction, respectively.

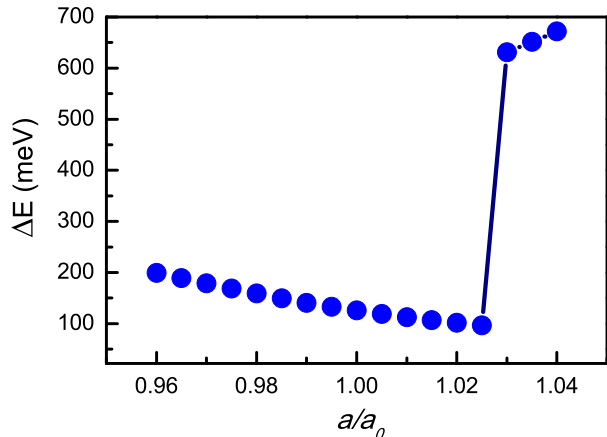


FIG. 4. (Color online) For VSiGeN<sub>4</sub> monolayer, the energy differences  $\Delta E$  between AFM and FM ordering as a function of  $a/a_0$ .

shall give our discussion and conclusion.

## II. COMPUTATIONAL DETAIL

Within density-functional theory (DFT)<sup>18</sup>, we perform spin-polarized first-principles calculations by employing the projected augmented wave method, as implemented in VASP code<sup>19–21</sup>. The generalized gradient approximation of Perdew-Burke-Ernzerhof (PBE-GGA)<sup>22</sup> is adopted as exchange-correlation functional. The energy cut-off of 500 eV, total energy convergence criterion of  $10^{-8}$  eV and force convergence criteria of less than  $0.0001 \text{ eV} \cdot \text{\AA}^{-1}$  on each atom are used to attain accurate results. A vacuum space of more than 30  $\text{\AA}$  is used to avoid the interactions between the neighboring slabs. The  $\Gamma$ -centered  $16 \times 16 \times 1$  k-point meshes are sampled in the Brillouin zone (BZ) for structure optimization, electronic structures and elastic stiffness tensor, and  $9 \times 16 \times 1$  Monkhorst-Pack k-point meshes for FM/antiferromagnetic (AFM) energy with rectangle supercell. The on-site Coulomb correlation of V atoms is considered by using GGA+ $U$  method within the rotationally invariant approach proposed by Dudarev et al<sup>23</sup>, and the  $U=3.2$  eV is used, which has been also used in

ref.<sup>17</sup>. The SOC effect is explicitly included to investigate MCA, electronic and topological properties of VSiGeN<sub>4</sub> monolayer.

The vibrational properties are investigated by the finite-displacement method with a  $5 \times 5 \times 1$  supercell, as implemented in the Phonopy code<sup>24</sup>. We use strain-stress relationship (SSR) to attain elastic stiffness tensor  $C_{ij}$ , and the 2D elastic coefficients  $C_{ij}^{2D}$  have been renormalized by  $C_{ij}^{2D} = L_z C_{ij}^{3D}$ , where the  $L_z$  is the cell height along  $z$  direction. The Berry curvatures are calculated directly from wave functions based on Fukui's method<sup>25</sup>, as implemented in VASPBERRY code<sup>26,27</sup>. The mostly localized Wannier functions including the  $d$ -orbitals of V atom and the  $p$ -orbitals of Si, Ge and N atoms are constructed on a k-mesh of  $16 \times 16 \times 1$ , and then are used to calculate edge states using Wannier90 and WannierTools packages<sup>28,29</sup>. The energy band structures of VSiGeN<sub>4</sub> calculated by DFT and fitted by Wannier90 at  $a/a_0=0.993$  (in topological state) are plotted in FIG.1 of electronic supplementary information (ESI), which confirms the fitting accuracy.

## III. STRUCTURE AND STABILITIES

As shown in **Figure 1**, this structure of VSiGeN<sub>4</sub> monolayer is stacked by seven atomic layers of N-Si-N-V-N-Ge-N. This can be regarded as a sandwich structure, and the middle VN<sub>2</sub> layer is sandwiched by SiN and GeN bilayers, which can be considered as a Janus structure. The VSiGeN<sub>4</sub> monolayer can be built by replacing the Si/Ge atoms of one of two SiN/GeN bilayers in VSi<sub>2</sub>N<sub>4</sub>/VGe<sub>2</sub>N<sub>4</sub> monolayer with Ge/N atoms. The symmetry of VSiGeN<sub>4</sub> (No.156) is lower than that of VSi<sub>2</sub>N<sub>4</sub>/VGe<sub>2</sub>N<sub>4</sub> (No.187) due to the lack of the reflection symmetry with respect to the middle VN<sub>2</sub> layer. The rhombus primitive cell and the rectangle supercell are plotted in **Figure 1** (a) along with AFM configuration, and the first BZ with high-symmetry points is shown in FIG.2 of ESI. The optimized lattice constants  $a$  of VSiGeN<sub>4</sub> monolayer is 2.959  $\text{\AA}$  with FM ordering, which agrees well with previous theoretical value (2.97 $\text{\AA}$ )<sup>17</sup>.

Our calculations show that VSiGeN<sub>4</sub> stabilizes into a FM ground state, and the FM state is 125.7 meV lower in energy than its AFM state with rectangle supercell. The

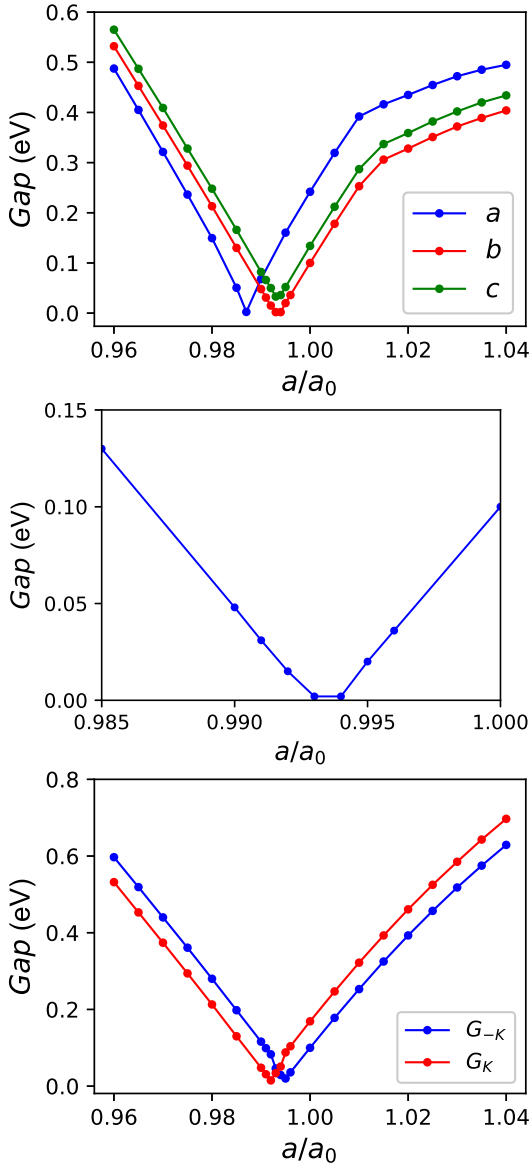


FIG. 5. (Color online) Top panel: the global energy band gap without SOC (a) and with SOC [out-of-plane magnetic anisotropy (b) and in-plane magnetic anisotropy (c)]; Middle panel: the enlarged view of global energy band gap with SOC [out-of-plane magnetic anisotropy] near  $a/a_0=0.993$ ; Bottom panel: the energy band gaps for -K and K valleys as a function of  $a/a_0$  with SOC [out-of-plane magnetic anisotropy].

MAE includes two main terms<sup>30–33</sup>: (1) MCA energy ( $E_{MCA}$ ), which is induced by the SOC, and (2) MSA energy ( $E_{MSA}$ ), which is due to the dipole-dipole (D-D) interaction:

$$E_{D-D} = -\frac{1}{2} \frac{\mu_0}{4\pi} \sum_{i \neq j} \frac{1}{r_{ij}^3} [\vec{M}_i \cdot \vec{M}_j - \frac{3}{2} (\vec{M}_i \cdot \vec{r}_{ij})(\vec{M}_j \cdot \vec{r}_{ij})] \quad (1)$$

where the  $\vec{M}_i$  represents the local magnetic moments and  $\vec{r}_{ij}$  are vectors that connect the sites  $i$  and  $j$ . The  $E_{MCA}$  is calculated from a energy difference be-

tween in-plane magnetization and out-of-plane magnetic anisotropy within SOC. The calculated  $E_{MCA}$  of VSiGeN<sub>4</sub> is only  $-3 \mu\text{eV}$ . For most materials, the magnetic D-D interaction is small compared with the MCA interaction. However, for VSiGeN<sub>4</sub>, it may play an important role due to very small  $E_{MCA}$ . According to Equation 1, the  $E_{MSA}$  is calculated from a energy difference with the magnetization rotating from the in-plane direction to the out-of-plane direction. The calculated  $E_{MSA}$  is  $-17 \mu\text{eV}$ , which dominates the MAE ( $-20 \mu\text{eV}$ ). The positive/negative MAE means that the easy magnetization axis is perpendicular/parallel to the plane of monolayer. The calculated MAE indicates in-plane easy magnetization, which means that there is no energetic barrier to the rotation of magnetization in the  $xy$  plane<sup>34</sup>. So, the VSiGeN<sub>4</sub> can be considered as a 2D XY magnet<sup>34,35</sup>. For a 2D XY magnet with a typical triangle lattice structure, a Berezinskii-Kosterlitz-Thouless magnetic transition to a quasi-long-range phase will produce at a critical temperature. The Monte Carlo simulations have predicted the critical temperature  $T_C = 1.335 \frac{J}{K_B}$ <sup>36,37</sup>, where  $J$  is the nearest-neighboring exchange parameter and  $K_B$  is the Boltzmann constant. The  $J$  is determined from the energy difference between AFM ( $E_{AFM}$ ) and FM ( $E_{FM}$ ). Based on the FM and AFM configurations, the AFM and FM energies can be obtained by equations:

$$E_{FM} = E_0 - (6J + 2A)S^2 \quad (2)$$

$$E_{AFM} = E_0 + (2J - 2A)S^2 \quad (3)$$

where  $E_0$  is the total energy of systems without magnetic coupling, and  $A$  describes the easy-axis single-ion anisotropy. The corresponding  $J$  can be attained:

$$J = \frac{E_{AFM} - E_{FM}}{8S^2} \quad (4)$$

The calculated  $J$  is 31.43 meV ( $S = \frac{1}{2}$ ), and the  $T_C$  is estimated to be 487 K.

The dynamical stability of VSiGeN<sub>4</sub> is verified by its phonon band dispersion, which is presented in Figure 1 (c). Phonon branches show no imaginary frequencies, indicating the dynamical stability of VSiGeN<sub>4</sub>. Ab initio molecular dynamics (AIMD) simulations are further performed to examine the thermal stability of VSiGeN<sub>4</sub> on a  $4 \times 4 \times 1$  supercell with a Nose thermostat of 300 K and a step time of 1 fs. As shown in Figure 1 (d), during the 8 ps simulation time, the energy are fluctuated around the equilibrium values without any sudden changes with small distortions in the final configurations, indicating its good thermal stability. The VSiGeN<sub>4</sub> has two independent elastic constants of  $C_{11}$  and  $C_{12}$ . If they satisfy Born criteria of  $C_{11} > 0$  and  $C_{11} - C_{12} > 0$ <sup>38,39</sup>, the VSiGeN<sub>4</sub> will be mechanically stable. The calculated two independent elastic constants of VSiGeN<sub>4</sub> are  $C_{11}=434.15 \text{ Nm}^{-1}$  and  $C_{12}=125.39 \text{ Nm}^{-1}$ , which satisfy the Born criteria of mechanical stability, confirming its mechanical stability.

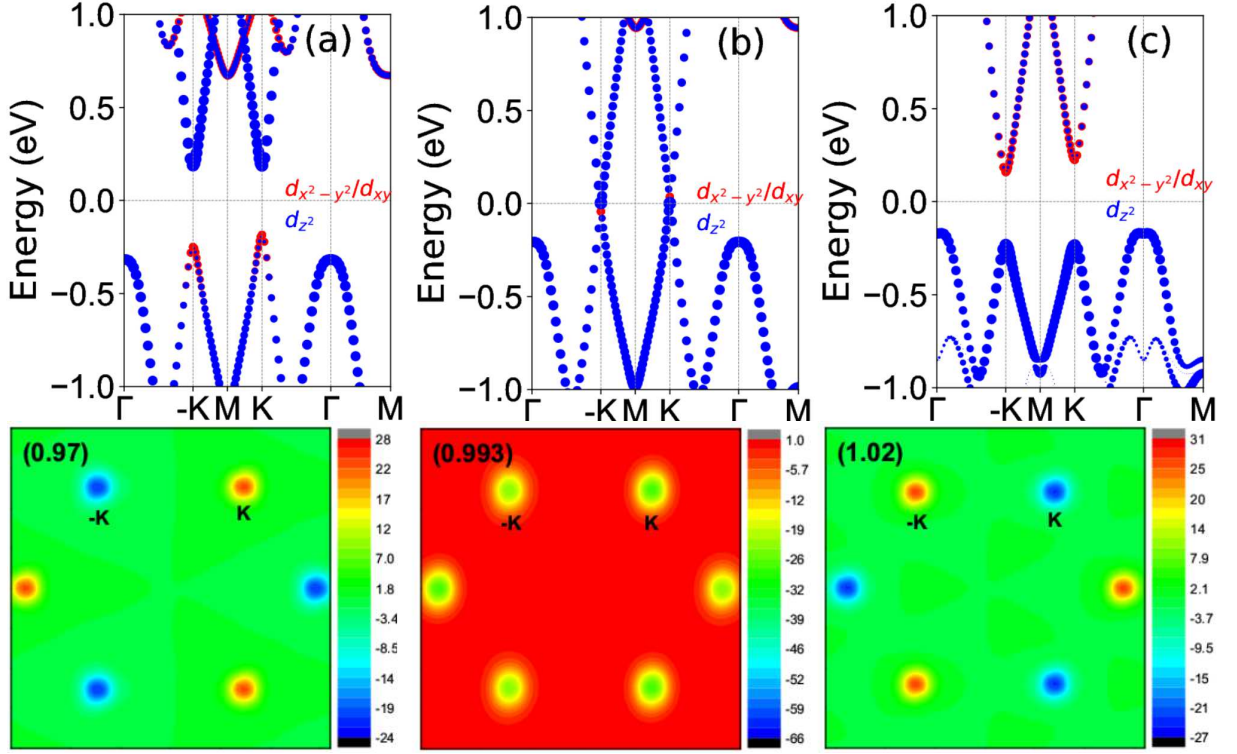


FIG. 6. (Color online) For VSiGeN<sub>4</sub> monolayer with out-of-plane magnetic anisotropy, the V- $d_{x^2-y^2}+d_{xy}$  and  $d_{z^2}$ -orbital characters energy band structures at representative  $a/a_0=0.97$  (a), 0.993 (b) and 1.02 (c), along with the corresponding Berry curvature distribution in 2D BZ.

#### IV. ELECTRONIC STRUCTURES

The magnetic anisotropy has crucial effects on the electronic states of 2D materials<sup>4-7</sup>. It is well known that the magnetization is a pseudovector. And then, the out-of-plane FM breaks all possible vertical mirrors of the system, but preserves the horizontal mirror symmetry. The preserved horizontal mirror symmetry allows the spontaneous valley polarization and a nonvanishing Chern number of a 2D system<sup>4</sup>. Although the magnetocrystalline direction of VSiGeN<sub>4</sub> monolayer is in-plane, this can be easily regulated into out-of-plane by external magnetic field due to the very small MAE.

For VSiGeN<sub>4</sub> monolayer, the spin-polarized band structures by using both GGA+ $U$  and GGA+ $U$ +SOC are shown in Figure 2. Figure 2 (a) shows a distinct spin splitting due to the exchange interaction, and VSiGeN<sub>4</sub> is a direct narrow band gap semiconductor with gap value of 0.242 eV. The valence band maximum (VBM) and conduction band bottom (CBM) are at K/-K point, which are provided by the spin-up. The energies of -K and K valleys are degenerate for both conduction and valence bands. The V- $d$  orbitals lie in a trigonal prismatic crystal field environment, and the  $d$  orbitals split into low-lying  $d_z^2$  orbital,  $d_{xy}+d_{x^2-y^2}$  and  $d_{xz}+d_{yz}$  orbitals. According to projected band structure in FIG.3 of ESI, only top  $d_{z^2}$ -dominated valence band in spin-up direction is occupied by one electron. This is expected to lead to a magnetic

moment of the 1  $\mu_B$  for each V atom, which conforms to the calculated value of 1.1  $\mu_B$ .

When including SOC, the valley polarization can be induced with out-of-plane magnetic anisotropy, as shown in Figure 2 (b). The valley splitting of bottom conduction band is 67 meV, while the valley splitting of top valence band is only 2 meV. For bottom conduction band, the energy of K valley is higher than that of -K valley. As plotted in Figure 2 (c), the valley polarization can be switched by reversing the magnetization direction (The energy of -K valley is higher than one of K valley.). Figure 2 (b) and (c) show that the gap value of VSiGeN<sub>4</sub> is about 0.10 eV. Based on Figure 2 (d), no valley polarization can be observed with in-plane magnetic anisotropy, and it is still a direct band gap semiconductor (0.134 eV).

FIG.3 of ESI show that the  $d_{x^2-y^2}+d_{xy}/d_z^2$  orbitals dominate -K and K valleys of bottom conduction band/top valence band, which determines the strength of valley splitting. The intra-atomic interaction  $\hat{H}_{SOC}^0$  from SOC mainly gives rise to valley polarization, which with out-of-plane magnetization can be expressed as<sup>40-42</sup>:

$$\hat{H}_{SOC}^0 = \alpha \hat{L}_z \quad (5)$$

where  $\hat{L}_z/\alpha$  is the orbital angular momentum along  $z$  direction/coupling strength. The resulting energy of K or -K

valley can be written as:

$$E^\tau = \langle \phi^\tau | \hat{H}_{SOC}^0 | \phi^\tau \rangle \quad (6)$$

where  $|\phi^\tau\rangle$  (subscript  $\tau = \pm 1$  as valley index) means the orbital basis for -K or K valley. If  $d_{x^2-y^2}+d_{xy}$  orbitals dominate -K and K valleys, the valley splitting  $|\Delta E|$  can be written as:

$$|\Delta E| = E^K - E^{-K} = 4\alpha \quad (7)$$

If the -K and K valleys are mainly from  $d_{z^2}$  orbitals, the valley splitting  $|\Delta E|$  is written as:

$$|\Delta E| = E^K - E^{-K} = 0 \quad (8)$$

According to FIG.3 of ESI, the valley splitting of bottom conduction band will be very large, and the valley splitting of top valence band will be very small, which agree well with our calculated results. With general magnetization orientation,  $\Delta E = 4\alpha \cos\theta$ <sup>42</sup> ( $\theta=0/90^\circ$  denotes out-of-plane/in-plane direction.) for  $d_{x^2-y^2}+d_{xy}$ -dominated -K/K valley. For in-plane one, the valley splitting of VSiGeN<sub>4</sub> will be zero.

When an in-plane longitudinal electric field  $E$  is applied, Bloch electrons can attain anomalous velocity  $v$ , which is associated with Berry curvature  $\Omega(k): v \sim E \times \Omega(k)$ <sup>43</sup>. The calculated Berry curvature of VSiGeN<sub>4</sub> as a contour map in 2D BZ with and without SOC are plotted in Figure 3, and their hot spots are around -K and K valleys. The four situations all show that Berry curvatures have opposite signs around -K and K valleys with equal/unequal magnitudes for valley-nonpolarized/valley-polarized situation. When reversing the magnetization from  $z$  to  $-z$  direction, the signs of Berry curvature at -K and K valleys remain unchanged, but their magnitudes exchange to each other. When the Fermi level falls between the -K and K valleys with appropriate electron doping, the Berry curvature forces the spin-up carriers of K valley to accumulate on one side of the sample by an applied in-plane electric field, giving rise to an anomalous valley Hall effect (AVHE). When the magnetization is reversed, the spin-down carriers of -K valley move to another side of the sample due to opposite Berry curvature compared with one of K valley.

## V. STRAIN EFFECTS

Strain is an effective method to tune the electronic state of some 2D materials, and can produce novel electronic states, such as FV, QAH and HVM states<sup>7,9,10</sup>. We use  $a/a_0$  to simulate the biaxial strain, where  $a/a_0$  are the strained/unstrained lattice constants. Here, both compressive ( $a/a_0 < 1$ ) and tensile ( $a/a_0 > 1$ ) strains are applied to achieve electronic states tuning ( $a/a_0: 0.96 \sim 1.04$ ). As shown in Figure 4, the total energy differences between AFM and FM ordering by using rectangle supercell indicate that the FM state is

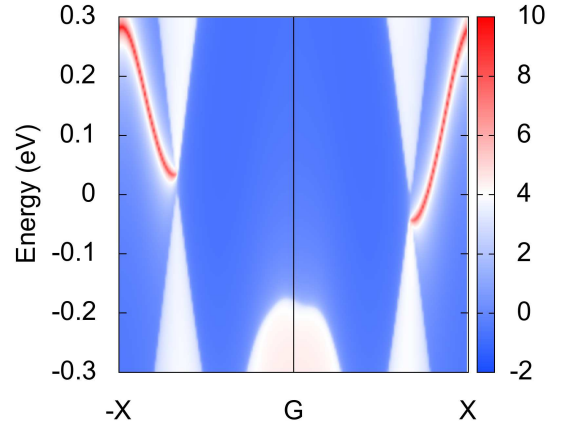


FIG. 7. (Color online) For VSiGeN<sub>4</sub> monolayer with out-of-plane magnetic anisotropy, the topological edge states at representative  $a/a_0=0.993$ .

always the magnetic ground state of VSiGeN<sub>4</sub> in considered strain range. It is found that total energy differences between AFM and FM ordering at  $a/a_0=1.03$  has a sudden jump. To explain this, the energies of AFM and FM ordering as a function of  $a/a_0$  are plotted in FIG.4 of ESI. Calculated results show that the energy of AFM ordering suddenly increases at  $a/a_0=1.03$ . To further reveal the underlying causes, the magnetic moments of V atom for both AFM and FM ordering as a function of  $a/a_0$  are plotted in FIG.5 of ESI. The energy difference jump is due to an abrupt change of the magnetic moment of V atom for AFM ordering, which reduces the magnetic interaction energy.

Next, the strain effects on electronic structures of VSiGeN<sub>4</sub> are investigated. Firstly, the total energy band gaps as a function of  $a/a_0$  without SOC are plotted in Figure 5, and energy band structures at some representative  $a/a_0$  values are shown in FIG.6 of ESI. When the  $a/a_0$  changes from 0.96 to 1.04, the gap firstly closes at about  $a/a_0=0.987$ , and then continues to increase. Before the energy gap closes, VSiGeN<sub>4</sub> is a direct gap semiconductor with VBM (CBM) at K/-K point. When  $a/a_0 > 0.987$ , VSiGeN<sub>4</sub> is still a direct gap semiconductor at small  $a/a_0$ . When  $a/a_0 > 1.01$ , VSiGeN<sub>4</sub> is an indirect gap semiconductor. The CBM is at the K/-K point, whereas the VBM deviates slightly from  $\Gamma$  point. In considered strain range, the K and -K valleys are always provided by the spin-up.

When including SOC, the magnetic anisotropy has crucial effects on electronic structures of VSiGeN<sub>4</sub>. Firstly, we consider that the magnetocrystalline direction of VSiGeN<sub>4</sub> is along out-of-plane. At some representative  $a/a_0$  values, the energy band structures with GGA+U+SOC are plotted in FIG.7 of ESI, and the evolutions of total energy band gap along with those at -K/K point vs  $a/a_0$  are shown in Figure 5. Calculated results show that there are two points around about  $a/a_0=0.9925$  and  $0.9945$ , where the total energy band gap is closed. At the two strain points, conduction

electrons are intrinsically 100% valley polarized, and the HVM state can be realized<sup>44</sup>. At about  $a/a_0=0.9925$ , the band gap of K valley gets closed, while a band gap at -K valley can be observed. At about  $a/a_0=0.9945$ , the band gap at -K valley is zero, while the band gap of K valley is kept. The considered strain ( $a/a_0$ ) region can be divided into three parts by two HVM electronic states.

It is found that K and -K valleys of both valence and conduction bands are primarily contributed by the  $d_{x^2-y^2}+d_{xy}$  or  $d_{z^2}$  orbitals of V atoms, and the orbital characters energy band structures at representative  $a/a_0=0.97, 0.993$  and  $1.02$  from three regions are plotted in Figure 6. For  $0.96 < a/a_0 < 0.9925$ , the  $d_{x^2-y^2}+d_{xy}$  orbitals dominate K and -K valleys of valence bands, while the two valleys of conduction bands are mainly from  $d_{z^2}$  orbitals (For example  $a/a_0=0.97$ ). When  $a/a_0$  is between  $0.9925$  and  $0.9945$ , the  $d_{x^2-y^2}+d_{xy}/d_{z^2}$  orbitals dominate K valleys of conduction/valence bands, while orbital characters of -K valley remain unchanged (For example  $a/a_0=0.993$ ). For  $0.9945 < a/a_0 < 1.04$ , the distributions of  $d_{x^2-y^2}+d_{xy}$  and  $d_{z^2}$  orbitals are opposite to ones of  $0.96 < a/a_0 < 0.9925$  (For example  $a/a_0=1.02$ ). These mean that there are two-time band inversion between  $d_{xy}+d_{x^2-y^2}$  and  $d_{z^2}$  orbitals with increasing  $a/a_0$ . The first occurs at K valley, accompanied by the first HVM state. The second band inversion occurs at -K valley, along with the second HVM state.

The two HVM states imply that the total gap of VSiGeN<sub>4</sub> closes and reopens two times, which suggests topological phase transition along with band inversion between  $d_{xy}+d_{x^2-y^2}$  and  $d_{z^2}$  orbitals. The QAH state may appear, when  $a/a_0$  is between  $0.9925$  and  $0.9945$ . The edge states at representative  $a/a_0=0.993$  are calculated to confirm QAH phase, which is plotted in Figure 7. It is clearly seen that a nontrivial chiral edge state connects the conduction bands and valence bands, implying a QAH phase. The calculated Chern number  $C=-1$ , which is also obtained by integrating the Berry curvature (see Figure 6) within the first BZ. There are no nontrivial chiral edge states for the other two regions ( $0.96 < a/a_0 < 0.9925$  and  $0.9945 < a/a_0 < 1.04$ ). With increasing  $a/a_0$ , two-time topological phase transitions can be observed in monolayer VSiGeN<sub>4</sub>.

The transformations of Berry curvatures of K and -K valleys are related with these topological phase transitions, and the distributions of Berry curvature are plotted in Figure 6 at representative  $a/a_0 = 0.97, 0.993$  and  $1.02$ . For  $0.96 < a/a_0 < 0.9925$  and  $0.9945 < a/a_0 < 1.04$ , the Berry curvatures around -K and K valleys have the opposite signs and different magnitudes. However, for  $0.9925 < a/a_0 < 0.9945$ , the same signs and different magnitudes can be observed for Berry curvatures around -K and K valleys. When  $a/a_0$  changes from  $0.96$  to  $1.04$ , there are twice topological phase transitions, which are related the flipping of the sign of Berry curvature at -K or K valley. For the first topological phase transitions, the positive Berry curvature ( $a/a_0=0.97$ ) changes into negative one ( $a/a_0=0.993$ ) at K valley. The second

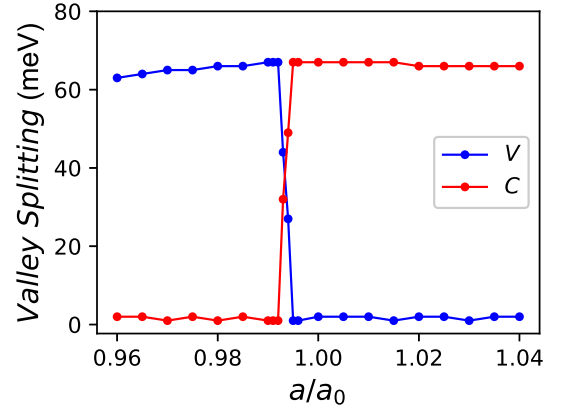


FIG. 8. (Color online) For VSiGeN<sub>4</sub> monolayer with out-of-plane magnetic anisotropy, the absolute value of valley splitting in both conduction (C) and valence (V) bands as a function of  $a/a_0$ .

topological phase transition is related with the sign flipping of Berry curvature of -K valley, and the negative Berry curvature ( $a/a_0=0.993$ ) changes into positive one ( $a/a_0=1.02$ ). These suggest that strain can induce sign-reversible Berry curvature at K or -K valley, and this is relevant to topological phase transition.

Calculated results show that VSiGeN<sub>4</sub> monolayer has spontaneous valley polarization, and the valley splitting for both valence and conduction bands is plotted in Figure 8. For  $0.96 < a/a_0 < 0.9925$ , the valley splitting of valence band is noteworthy, while the valley splitting of conduction band is very small. However, for  $0.9945 < a/a_0 < 1.04$ , the opposite situation can be observed for valley splitting, compared with the case of  $0.96 < a/a_0 < 0.9925$ . These can be explained by the distributions of  $d_{x^2-y^2}+d_{xy}$  and  $d_{z^2}$  orbitals (see Figure 6). If  $d_{x^2-y^2}+d_{xy}/d_{z^2}$  orbitals dominate -K and K valleys, the valley splitting will be large/small. For  $0.9925 < a/a_0 < 0.9945$ , the valley splitting for both valence and conduction bands is observable. In this region, VSiGeN<sub>4</sub> is a VQAH with spontaneous valley splitting and chiral edge states. For VAQHI, the edge state has a special behavior of chiral-spin-valley locking. For example  $a/a_0=0.993$ , the edge state in Figure 7 is spin up with 100% spin polarization and 100% valley polarization, which is because the bands near the Fermi level are dominated by spin-up bands. The edge state only appears at the K valley due to the flipping of the sign of the Berry curvature or band inversion at K valley. When the magnetization is reversed, the edge state will move to the -K valley with an opposite spin direction and chiral.

In quick succession, we suppose the magnetocrystalline direction of VSiGeN<sub>4</sub> monolayer along in-plane one. The energy band gaps as a function of  $a/a_0$  are plotted in Figure 5, and the representative energy band structures are shown in FIG.8 of ESI. When  $a/a_0$  changes from  $0.96$  to  $1.04$ , the gap firstly decreases, and then increases. The corresponding  $a/a_0$  of gap close is about  $0.993$ . It

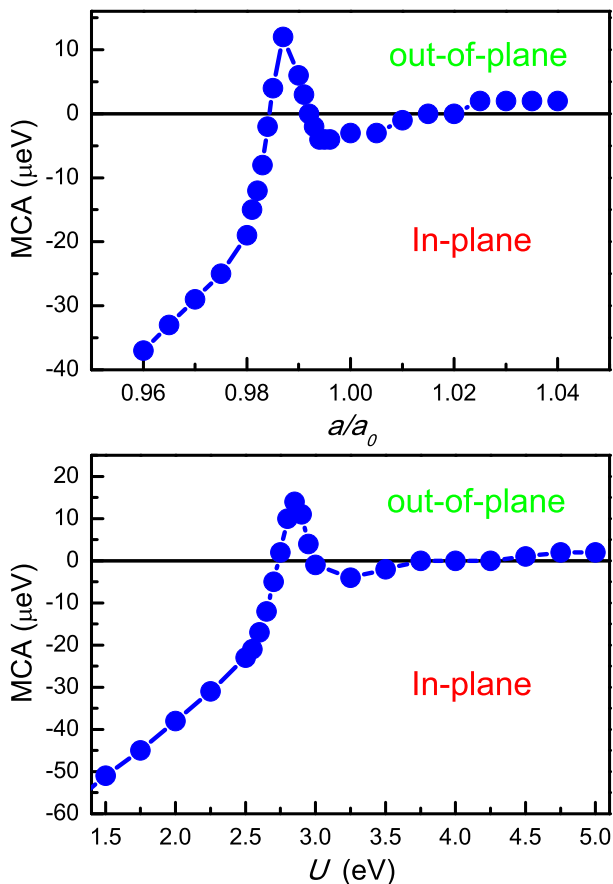


FIG. 9. (Color online) For VSiGeN<sub>4</sub> monolayer, the MCA energy as a function of  $a/a_0$  (Top plane) and  $U$  (Bottom plane).

is found that no spontaneous valley polarization in both valence and conduction bands can be observed, and no QAH phase can be induced by strain. When  $a/a_0$  is less than about 1.01 except 0.993 (semimetal), VSiGeN<sub>4</sub> is a direct gap semiconductor with VBM (CBM) at K/-K point. When  $a/a_0 > 1.01$ , VSiGeN<sub>4</sub> is a indirect gap semiconductor with CBM at the K/-K points, and the VBM deviates slightly from  $\Gamma$  point. In short, VSiGeN<sub>4</sub> monolayer is a common FM semiconductor or semimetal.

Finally, we investigate the strain effects on MAE of VSiGeN<sub>4</sub>. We plot the MCA energy as a function of  $a/a_0$  in Figure 9. Strain-driven complex MCA (multiple transitions in the MCA) can be observed. In considered strain range, the MSA energy changes from  $-19 \mu\text{eV}$  to  $-17 \mu\text{eV}$  to  $-15 \mu\text{eV}$ , when the  $a/a_0$  changes from 0.96 to 1.00 to 1.04. Calculated results show that the MAE is always negative within considered strain range, which means that strained VSiGeN<sub>4</sub> is intrinsically common magnetic semiconductor. However, the magnetization can be adjusted from the in-plane to off-plane direction through overcoming a small energy barrier by the external magnetic field, which will produce valley polarization and

QAH phase. Within considered strain range, the largest energy barrier ( $56 \mu\text{eV}$  at  $a/a_0=0.96$ ) is equivalent to applying a external magnetic field of around 0.28-0.56 T.

## VI. DISCUSSION AND CONCLUSION

Monolayer RuBr<sub>2</sub> shows the same electronic states induced by strain with VSiGeN<sub>4</sub> for both out-of-plane and in-plane cases<sup>7</sup>. However, the MCA energy of RuBr<sub>2</sub> varies monotonously with increasing  $a/a_0$ . The strain can suppress/enhance the kinetic energy of electron, and then effectively enhances/suppresses the correlation effect<sup>5</sup>. This means that electronic correlation can induce the similar change of electronic states and MCA energy with strain, which has been confirmed for RuBr<sub>2</sub><sup>7</sup>. To further confirm complex strain dependence of MCA energy, we calculate the MCA energy as a function of correlation strength  $U$ , which is also plotted in Figure 9. It is clearly seen that the MCA vs  $a/a_0$  and MCA vs  $U$  show very similar behavior, as expected. The complex strain dependence of MCA can be readily extended to VSi<sub>2</sub>P<sub>4</sub>, VSi<sub>2</sub>N<sub>4</sub>, VSiSnN<sub>4</sub> and so on, because they share the same crystal structure with VSiGeN<sub>4</sub>. In fact, for VSi<sub>2</sub>P<sub>4</sub>, one can observe similar transitions in the MCA energy as a function of  $U$ <sup>5</sup>.

In summary, we have demonstrated that strain can result in a different phase diagram for different magnetic anisotropy (out-of-plane and in-plane cases). For out-of-plane situation, the strain can induce novel VQAH with exotic chiral-spin-valley locking edge states between two HVM states, and these are related with sign-reversible Berry curvature and band inversions of  $d_{xy}+d_{x^2-y^2}$  and  $d_{z^2}$  orbitals at -K and K valleys. For in-plane situation, VSiGeN<sub>4</sub> is a common magnetic semiconductor without spontaneous valley polarization. Particularly, the calculated intrinsic MCA energy shows multiple transitions induced by strain, which is further confirmed by calculating MCA vs  $U$ . Intrinsically, there is not a VQAH, which can be realized by external magnetic field. Our works deepen our understanding of strain effects in the V-based 2D MA<sub>2</sub>Z<sub>4</sub> family materials, and open new perspectives for multifunctional electronic device applications based on these materials.

## ACKNOWLEDGMENTS

This work is supported by Natural Science Basis Research Plan in Shaanxi Province of China (2021JM-456), Graduate Innovation Fund Project in Xi'an University of Posts and Telecommunications (CXJJDL2021001). We are grateful to Shanxi Supercomputing Center of China, and the calculations were performed on TianHe-2.

- 
- <sup>1</sup> N. D. Mermin and H. Wagner, *Phys. Rev. Lett.* **17**, 1133 (1966).
- <sup>2</sup> C. Gong, L. Li, Z. Li, H. Ji, A. Stern, Y. Xia, T. Cao, W. Bao, C. Wang, Y. Wang, Z. Q. Qiu, R. J. Cava, S. G. Louie, J. Xia and X. Zhang, *Nature* **546**, 265 (2017).
- <sup>3</sup> B. Huang, G. Clark, E. Navarro-Moratalla, D. R. Klein, R. Cheng, K. L. Seyler, D. Zhong, E. Schmidgall, M. A. McGuire, D. H. Cobden, W. Yao, D. Xiao, P. Jarillo-Herrero and X. Xu, *Nature* **546**, 270 (2017).
- <sup>4</sup> X. Liu, H. C. Hsu, and C. X. Liu, *Phys. Rev. Lett.* **111**, 086802 (2013).
- <sup>5</sup> S. Li, Q. Q. Wang, C. M. Zhang, P. Guo and S. A. Yang, *Phys. Rev. B* **104**, 085149 (2021).
- <sup>6</sup> S. D. Guo, J. X. Zhu, M. Y. Yin and B. G. Liu, *Phys. Rev. B* **105**, 104416 (2022).
- <sup>7</sup> S. D. Guo, W. Q. Mu and B. G. Liu, *2D Mater.* **9**, 035011 (2022).
- <sup>8</sup> S. Yang, Y. Chen and C. Jiang, *InfoMat.* **3**, 397 (2021).
- <sup>9</sup> Y. L. Wang and Y. Ding, *Appl. Phys. Lett.* **119**, 193101 (2021).
- <sup>10</sup> H. Huan, Y. Xue, B. Zhao, G. Y. Gao, H. R. Bao and Z. Q. Yang, *Phys. Rev. B* **104**, 165427 (2021).
- <sup>11</sup> Y. L. Hong, Z. B. Liu, L. Wang T. Y. Zhou, W. Ma, C. Xu, S. Feng, L. Chen, M. L. Chen, D. M. Sun, X. Q. Chen, H. M. Cheng and W. C. Ren, *Science* **369**, 670 (2020).
- <sup>12</sup> L. Wang, Y. Shi, M. Liu, A. Zhang, Y.-L. Hong, R. Li, Q. Gao, M. Chen, W. Ren, H.-M. Cheng, Y. Li, and X.-Q. Chen, *Nature Communications* **12**, 2361 (2021).
- <sup>13</sup> Q. Wang, L. Cao, S. J. Liang et al., *npj 2D Mater. Appl.* **5**, 71 (2021).
- <sup>14</sup> L. Cao, G. Zhou, Q. Wang L. K. Ang and Y. S. Ang, *Appl. Phys. Lett.* **118**, 013106 (2021).
- <sup>15</sup> S. D. Guo, W. Q. Mu, Y. T. Zhu, R. Y. Han and W. C. Ren, *J. Mater. Chem. C* **9**, 2464 (2021).
- <sup>16</sup> S. D. Guo, Y. T. Zhu, W. Q. Mu and X. Q. Chen, *J. Mater. Chem. C* **9**, 7465 (2021).
- <sup>17</sup> D. Dey, A. Ray and L. P. Yu, arXiv:2203.11605 (2022).
- <sup>18</sup> P. Hohenberg and W. Kohn, *Phys. Rev.* **136**, B864 (1964); W. Kohn and L. J. Sham, *Phys. Rev.* **140**, A1133 (1965).
- <sup>19</sup> G. Kresse, *J. Non-Cryst. Solids* **193**, 222 (1995).
- <sup>20</sup> G. Kresse and J. Furthmüller, *Comput. Mater. Sci.* **6**, **15** (1996).
- <sup>21</sup> G. Kresse and D. Joubert, *Phys. Rev. B* **59**, 1758 (1999).
- <sup>22</sup> J. P. Perdew, K. Burke and M. Ernzerhof, *Phys. Rev. Lett.* **77**, 3865 (1996).
- <sup>23</sup> S. L. Dudarev, G. A. Botton, S. Y. Savrasov, C. J. Humphreys and A. P. Sutton, *Phys. Rev. B* **57**, 1505 (1998).
- <sup>24</sup> A. Togo, F. Oba, and I. Tanaka, *Phys. Rev. B* **78**, 134106 (2008).
- <sup>25</sup> T. Fukui, Y. Hatsugai and H. Suzuki, *J. Phys. Soc. Japan.* **74**, 1674 (2005).
- <sup>26</sup> H. J. Kim, <https://github.com/Infant83/VASPBERRY>, (2018).
- <sup>27</sup> H. J. Kim, C. Li, J. Feng, J.-H. Cho, and Z. Zhang, *Phys. Rev. B* **93**, 041404(R) (2016).
- <sup>28</sup> A. A. Mostofia, J. R. Yatesb, G. Pizzif, Y.-S. Lee, I. Souza, D. Vanderbilt and N. Marzari, *Comput. Phys. Commun.* **185**, 2309 (2014).
- <sup>29</sup> Q. Wu, S. Zhang, H. F. Song, M. Troyer and A. A. Soluyanov, *Comput. Phys. Commun.* **224**, 405 (2018).
- <sup>30</sup> X. B. Lu, R. X. Fei, L. H. Zhu and L. Yang, *Nat. Commun.* **11**, 4724 (2020).
- <sup>31</sup> M. Akram, H. LaBollita, D. Dey, J. Kapeghian, O. Erten and A. S. Botana, *Nano Lett.* **21**, 6633 (2021).
- <sup>32</sup> H. J. F. Jansen, *Phys. Rev. B* **59**, 4699 (1999).
- <sup>33</sup> F. Xue, Y. Hou, Z. Wang and R. Wu, *Phys. Rev. B* **100**, 224429 (2019).
- <sup>34</sup> K. Sheng, Q. Chen, H. K. Yuan and Z. Y. Wang, *Phys. Rev. B* **105**, 075304 (2022).
- <sup>35</sup> J. L. Lado and J. Fernández-Rossier, *2D Mater.* **4**, 035002 (2017).
- <sup>36</sup> P. Jiang, L. Kang, Y.-L. Li, X. Zheng, Z. Zeng, and S. Sanvito, *Phys. Rev. B* **104**, 035430 (2021).
- <sup>37</sup> S. Zhang, R. Xu, W. Duan, and X. Zou, *Adv. Funct. Mater.* **29**, 1808380 (2019).
- <sup>38</sup> E. Cadelano and L. Colombo, *Phys. Rev. B* **85**, 245434 (2012).
- <sup>39</sup> Y. X. Wu, W. Sun, S. Y. Liu, B. Wang, C. Liu, H. B. Yin and Z. X. Cheng, *Nanoscale* **13**, 16564 (2021).
- <sup>40</sup> W. Y. Tong, S. J. Gong, X. Wan, and C. G. Duan, *Nat. Commun.* **7**, 13612 (2016).
- <sup>41</sup> P. Zhao, Y. Dai, H. Wang, B. B. Huang and Y. D. Ma, *ChemPhysMater*, **1**, 56 (2022).
- <sup>42</sup> R. Li, J. W. Jiang, W. B. Mi and H. L. Bai, *Nanoscale* **13**, 14807 (2021).
- <sup>43</sup> D. Xiao, M. C. Chang, and Q. Niu, *Rev. Mod. Phys.* **82**, 1959 (2010).
- <sup>44</sup> H. Hu, W. Y. Tong, Y. H. Shen, X. Wan, and C. G. Duan, *npj Comput. Mater.* **6**, 129 (2020).